GEOPHYSICS, VOL. 82, NO. 6 (NOVEMBER-DECEMBER 2017); P. JM23–JM36, 10 FIGS.
10.1190/GEO2016-0567.1

Accounting for relaxation during pulse effects for long pulses and fast relaxation times in surface nuclear magnetic resonance

Denys Grombacher[1], Ahmad A. Behroozmand[2], and Esben Auken[1]

ABSTRACT

Surface nuclear magnetic resonance (NMR) is a geophysical technique providing noninvasive insight into aquifer properties. To ensure that reliable water content estimates are produced, accurate modeling of the excitation process is necessary. This requires that relaxation during pulse (RDP) effects be accounted for because they may lead to biased water content estimates if neglected. In surface NMR, RDP is not directly included into the excitation modeling, rather it is accounted for by adjusting the time at which the initial amplitude of the signal is calculated. Previous work has demonstrated that estimating the initial amplitude of the signal as the value obtained by extrapolating the observed signal to the middle of the pulse can greatly improve performance for the on-resonance pulse. To better understand the reliability of these types of approaches (which do not directly include RDP in the modeling), the performance of these approaches is tested using numerical simulations for a broad range of conditions, including for multiple excitation pulse types. Hardware advances that now allow the routine measurement of much faster relaxation times (where these types of approaches may lead to poor water content estimates) and a recent desire to use alternative transmit schemes demand a flexible protocol to account for RDP effects in the presence of fast relaxation times for arbitrary excitation pulses. To facilitate such a protocol, an approach involving direct modeling of RDP effects using estimates of the subsurface relaxation times is presented to provide more robust and accurate water content estimates under conditions representative of surface NMR.

INTRODUCTION

Surface nuclear magnetic resonance (NMR) is a geophysical technique providing noninvasive characterization of aquifer properties (Legchenko and Valla, 2002). During a surface NMR measurement, surface coils are used to first perturb a magnetization present at depth (that originates from the immersion of hydrogen nuclei in the earth's magnetic field) and subsequently measure this magnetization's return to equilibrium. The perturbation of the magnetization is accomplished by pulsing an AC current in a surface coil that oscillates at or near the precessional frequency of the magnetization (called the Larmor frequency ω_0) for a short duration, typically 20–40 ms. The oscillatory current generates a secondary magnetic field at depth (called the B_1 field) that perturbs the magnetization out of its equilibrium orientation, allowing a surface coil to inductively measure the properties of the magnetization. The amplitude of the measured magnetization and the rate at which it returns to equilibrium (called the decay rate) provide insight into aquifer properties such as water content (related to the amplitude; Legchenko and Valla, 2002), pore sizes, and permeability (related to the decay rate; Kenyon et al., 1988; Mohnke and Yaramanci, 2008).

To ensure that surface NMR produces reliable aquifer characterizations, accurate modeling of the excitation process is needed. This requires the following: (1) a model of the spatially varying B_1 responsible for perturbing the magnetization. An accurate B_1 model is essential to determine the spatial origin of the measured signal. Accounting for the effects of a conductive subsurface on B_1 also improves the modeling of the signal phase (Trushkin et al., 1995; Shushakov, 1996a). This allows inversion schemes handling complex NMR data (Braun et al., 2005) and/or joint-inversion schemes integrating time-domain electromagnetics (TEM) and surface NMR data (Behroozmand et al., 2012) to be exploited to improve the spatial

Manuscript received by the Editor 4 November 2016; revised manuscript received 8 April 2017; published ahead of production 01 August 2017; published online 25 September 2017.
[1]Aarhus University, Department of Geoscience, Aarhus, Denmark. E-mail: denys.grombacher@geo.au.dk; esben.auken@geo.au.dk.
[2]Stanford University, Geophysics Department, Stanford, California, USA. E-mail: abehrooz@stanford.edu.

resolution of surface NMR depth profiles. (2) Reliable Larmor frequency estimates (Walbrecker et al., 2011a; Grombacher and Knight, 2015) because uncertain Larmor frequency estimates may lead to the presence of off-resonance effects that impact the signal's amplitude, phase, and spatial origin. If neglected, these effects may reduce the accuracy of estimated water content profiles (Grombacher and Knight, 2015) and cause the appearance of ghost aquifers at depth (Legchenko, 2005). (3) Methods to account for processes that act to return the magnetization to equilibrium during the excitation pulse (these processes are referred to as relaxation during pulse [RDP]; Walbrecker et al., 2009). If neglected, RDP may reduce the accuracy of estimated water contents.

The focus of this paper is the impact of RDP in surface NMR, specifically in the limit in which the relaxation times are on the order of the pulse duration. This scenario (fast relaxation times) is common in the vadose zone (Costabel and Yaramanci, 2011a), magnetic environments (Grunewald and Knight, 2012), and for regions containing fine sands or clays (Schirov et al., 1991). In the magnetic resonance imaging (MRI) literature RDP is known to impact the performance of excitation pulses for short relaxation times (Norris et al., 1991; Raddi and Klose, 2000). Hajduk et al. (1993) demonstrate that RDP depends strongly on the type of the excitation pulse. As such, one strategy to account for RDP in MRI is to design excitation pulses inherently less sensitive to RDP, in which the pulse waveform is determined using an optimal control (Gershenzon et al., 2007) or simulated annealing (Nuzillard and Freeman, 1993; Shen and Lerner, 1994) scheme. However, such a strategy does not easily translate to surface NMR. This is partly due to limitations on the complexity of excitation pulse waveforms currently feasible in surface NMR, but primarily because RDP concerns in surface NMR are somewhat different than in MRI. In MRI, the concern is often the impact of RDP on the excitation slice profile (Hajduk et al., 1993), whereas for surface NMR, the primary concern is the ability of the forward model to reliably reproduce the observed signal amplitudes using the correct subsurface water content (Walbrecker et al., 2009). The reason for this difference is due to the differing way images are formed in MRI versus surface NMR. The spatial encoding of the signal origin is far more precisely controlled by the pulse in MRI than in surface NMR, in which an inversion is required to estimate the subsurface water content. Therefore, the focus on RDP in surface NMR has not been to implement RDP insensitive pulses but rather to develop schemes to account for RDP allowing estimation of more reliable water contents. Two schemes have been used in surface NMR to deal with RDP; in the following, we will refer to these schemes as the extrapolation to end-pulse (EEP) and extrapolation to mid-pulse (EMP) approaches (Walbrecker et al., 2009). Neither approach directly includes RDP during excitation modeling. Instead, an attempt to account for RDP is made by adjusting the time at which the initial amplitude of the signal is calculated. The aim of these approaches is to calculate the initial amplitude at a time when the signal amplitude is roughly equivalent to that which would have been produced in the absence of RDP effects. The EEP approach, which calculates the initial amplitude by extrapolating the observed decay to the end of the pulse, is known to break down in the fast relaxation time limit (Walbrecker et al., 2009). To improve upon the EEP approach, Weichman et al. (2000) propose the EMP approach, in which the initial amplitude is estimated by extrapolating the observed signal to the middle of the pulse. Walbrecker et al. (2009) investigate the EMP approach in detail, finding that it greatly improves performance compared with the EEP approach, and it is reliable for effective transverse relaxation times (T_2^*) greater than roughly one to two times the pulse duration τ. However, Walbrecker et al. (2009) test the EMP approach for a single excitation pulse type (an on-resonance pulse), a single B_1 amplitude (which corresponded to a $\pi/2$ pulse), and the homogeneous background magnetic field (B_0) limit (the $T_2^* = T_2$ limit). In the following, the EEP and EMP approaches are tested for a greater range of conditions, including a larger B_1 range, multiple excitation pulse types, and for homogeneous and inhomogeneous B_0 cases.

Recent hardware advancements, focused on reducing the dead time (t_{dead}) (Walsh et al., 2011; Li et al., 2015), now make it feasible to consistently measure fast relaxation times that do not fall in the $T_2^* \gg \tau$ regime (where the EEP and EMP approach are known to break down). Reliable results in the presence of fast relaxation times are essential for surface NMR investigations of vadose zone processes (Costabel and Yaramanci, 2011a, 2011b), magnetic settings (Roy et al., 2008; Grunewald and Knight, 2011), and fine sands/clayey environments (Sen et al., 1990; Schirov et al., 1991). In addition, growing interest in the use of alternative transmit schemes in surface NMR, such as composite pulses (Grombacher et al., 2014) or adiabatic pulses (Grunewald et al., 2016), requiring longer pulse durations also necessitates the development of a scheme to handle RDP for a broader range of relaxation times that is effective for an arbitrary excitation pulse type.

To provide such a scheme, we propose to update the surface NMR forward model using information available from the observed NMR signals to directly include RDP effects (referred to in the following as the model RDP [MRDP] approach). Relaxation times fit to the observed signals are used to update the forward model by resolving the Bloch equation (Bloch, 1946) with appropriately weighted relaxation terms present. We hypothesize that such a modeling approach has the potential to extend the range of conditions in which a reliable water content can be produced, while also improving the flexibility of the excitation modeling to weight RDP effects appropriately for the specific excitation pulse chosen, local B_1 amplitude, and local B_0 conditions (homogeneous versus inhomogeneous). Numerical results are presented to contrast the performance of the MRDP approach against the EEP and EMP schemes under conditions representative of the surface NMR experiment. A discussion about the limitations of the MRDP approach and a potential strategy for the integration of the MRDP scheme into the surface NMR workflow is also given.

BACKGROUND

Excitation modeling

To generate a measureable signal in surface NMR, the magnetization must be perturbed out of its equilibrium orientation along the earth's field direction and given a component transverse to this direction. To accomplish this, a secondary magnetic field is produced by pulsing a strong oscillatory current in a coil at the surface. In the presence of this secondary field, the perturbation of the magnetization is described by the Bloch (1946) equation:

$$\frac{d\mathbf{M}}{dt} = \gamma\mathbf{M} \times \mathbf{B}_{\mathbf{eff}} - \frac{\mathrm{M}_x}{T_2}\mathbf{x} - \frac{\mathrm{M}_y}{T_2}\mathbf{y} - \frac{\mathrm{M}_z - \mathrm{M}_0}{T_1}\mathbf{z}, \tag{1}$$

where $\mathbf{M}$ is the magnetization, $\mathbf{B}_{\mathbf{eff}}$ is the effective magnetic field experienced by the magnetization, and T_2 and T_1 are the transverse and longitudinal relaxation times, respectively. The γ term is the gyromagnetic ratio of the hydrogen nuclei. The M_x, M_y, and M_z terms refer to the x-, y-, and z-components of $\mathbf{M}$ in a reference frame where z is oriented along the direction of the background magnetic field B_0 (earth's field in the case of surface NMR). The terms $\mathbf{x}$, $\mathbf{y}$, and $\mathbf{z}$ are the unit vectors. The M_0 term is the magnitude of the magnetization at equilibrium. The cross-product indicates that the applied magnetic field induces a torque on the magnetization causing it to nutate about an axis oriented in the $\mathbf{B}_{\mathbf{eff}}$ direction, whereas the terms containing T_2 and T_1 correspond to the decay of the transverse magnetization (M_x and M_y) and the regrowth of the longitudinal magnetization (M_z), respectively. The relaxation terms act to return a perturbed magnetization back to its equilibrium orientation.

It is convenient to consider the perturbation of the magnetization in a reference frame that rotates at the instantaneous transmit frequency (ω_t) of the current in the surface coil. This reference frame (called the rotating-reference frame) is selected such that the z- and x-axes are oriented in the direction of the earth's field and the direction of the B_1-component perpendicular to earth's field, respectively. In the following, the use of B_1 refers to the corotating component of the secondary magnetic field perpendicular to the B_0 direction (Weichman et al., 2000). The term $\mathbf{B}_{\mathbf{eff}}$ in this frame is described by

$$\mathbf{B}_{\mathbf{eff}} = \begin{bmatrix} B_1 \\ 0 \\ (\omega_0 - \omega_t)/\gamma \end{bmatrix}. \tag{2}$$

Equations 1 and 2 illustrate that to model the perturbation of the magnetization, we require accurate knowledge of (1) the B_1 amplitude, (2) the difference between ω_0 and ω_t (called the offset), and (3) the relaxation times T_1 and T_2 at all locations in the subsurface. The B_1 distribution throughout the subsurface can be calculated given the coil size, coil geometry, and subsurface conductivity structure (the conductivity structure typically comes from a supplementary electrical resistivity tomography or TEM survey). The offset can be determined using a magnetometer to estimate ω_0, refined by viewing the NMR signal's spectrum, or compensated by using the frequency-cycling method (Grombacher et al., 2016) if the offset is unknown. The final parameters needed are the relaxation times, which are not known a priori. In the following, we assume that B_1 and the offset are accurately determined and focus only on the influence of the relaxation terms.

The free-induction decay

The standard surface NMR measurement is the free-induction decay (FID), which involves measuring the NMR signal following a single excitation pulse. The time dependence of the FID is described by the effective relaxation time T_2^*,

$$\frac{1}{T_2^*} = \frac{1}{T_2} + \frac{1}{T_{2\mathrm{IH}}}. \tag{3}$$

The term T_2 describes the signal loss due to surface relaxation and bulk relaxation, and it is the term that carries the link to pore geometry (Brownstein and Tarr, 1979) (the surface area to volume ratio of the pore space). The $T_{2\mathrm{IH}}$ term encompasses signal loss due to the presence of an inhomogeneous background magnetic field (B_0) (Chen et al., 2005; Grunewald and Knight, 2011). Inhomogeneous B_0 leads to a spatially varying Larmor frequency that causes magnetizations at different locations to dephase and accumulate relative phases with respect to one another. The accumulated phases result in destructive interference that accelerates the observed decay. Because an observed T_2^* value does not correspond to a unique T_2 and $T_{2\mathrm{IH}}$ pair, ambiguity exists about which of these two terms is most influential in determining T_2^*. Figure 1 illustrates this ambiguity, where T_2^* contours are shown for varying magnitudes of T_2 and $T_{2\mathrm{IH}}$ (curved light gray lines). Contours corresponding to T_2^* of 20 (closest to the bottom left corner), 40, 60, 100, 200, and 400 ms (closest to the top right corner), are shown. The dashed line illustrates the case where $T_{2\mathrm{IH}} = T_2$. Three regimes are present in Figure 1: (1) The $T_2{\sim} = T_2^*$ regime (the region below the dashed line in which the contour lines are roughly horizontal), which can be effectively considered as the homogeneous B_0 limit. (2) The $T_{2\mathrm{IH}}{\sim} = T_2^*$ regime (the region above the dashed line in which the contour lines are roughly vertical), which can be considered as the inhomogeneous B_0 case. (3) The mixed regime in which T_2 and $T_{2\mathrm{IH}}$ are similar in magnitude (the region near the dashed $T_{2\mathrm{IH}} = T_2$ line). In the following, we will refer to these regimes as the $T_2{\sim} = T_2^*$, the $T_{2\mathrm{IH}}$-dominated, and the mixed regimes, respectively.

The inability to determine which of the three regimes is present represents one of the primary shortcomings of the FID in surface NMR. Ideally, the observed T_2^* values could be used to gain insight into pore size and permeability, but this requires that the $T_2{\sim} = T_2^*$ regime be present. Unfortunately, this cannot be verified given only FID measurements. As a result, much research has focused on the development of alternative transmit approaches to directly measure relaxation times insensitive to $T_{2\mathrm{IH}}$ (such as T_2 and T_1) to ensure a strong link between the relaxation times and the pore geometry (Shushakov, 1996b; Legchenko et al., 2004, 2010; Walbrecker et al., 2011b; Grunewald and Walsh, 2013; Grunewald et al., 2014). However, despite the uncertainty about the meaning of T_2^* (i.e., which regime is present) the FID remains a staple measurement in surface

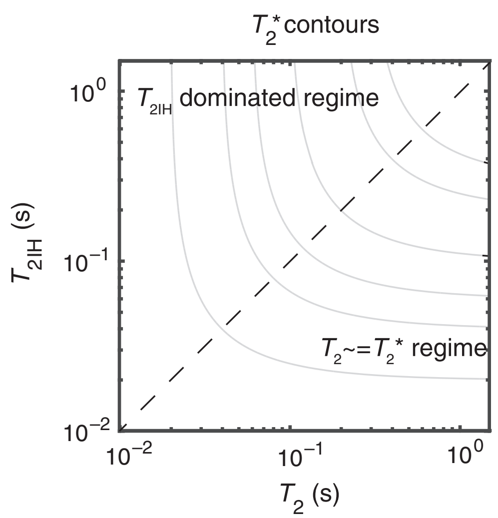

Figure 1. Schematic illustration of the dependence of T_2^* on T_2 and $T_{2\mathrm{IH}}$. The gray lines illustrate various T_2^* contours. Contours corresponding to T_2^* of 20 (closest to the bottom left corner), 40, 60, 100, 200, and 400 ms (closest to top right corner), are shown. The dashed line illustrates the case where $T_{2\mathrm{IH}} = T_2$. The $T_{2\mathrm{IH}}$-dominated regime corresponds to the upper left corner, whereas the $T_2{\sim} = T_2^*$ regime corresponds to the lower right corner.

NMR. The FID provides the greatest depth penetration and remains a robust pulse for producing images of the spatial distribution of the subsurface water content.

To illustrate how a water content estimate can be produced from an FID measurement, consider a simple toy problem in which a unit magnetization at equilibrium is perturbed by an excitation pulse and the subsequent decay of its transverse component is measured. In this case, the signal $\mathrm{M}(t)$ is described by

$$\mathrm{M}(t) = \mathrm{M}_0 m_\perp e^{-t/T_2^*}. \tag{4}$$

The goal is to determine the magnetization's equilibrium magnitude M_0. The magnitude of M_0 is related to the number of hydrogen nuclei present within the sensitive volume, which can be directly related to water content. If M_0 is accurately determined, a reliable water content estimate will be produced. The $m_\perp$ term describes the magnitude of the transverse magnetization produced by the excitation pulse given an initial condition described by a unit magnetization at equilibrium; $m_\perp = m_y + i m_x$, where m_x and m_y refer to the x- and y-components of a unit magnetization following the excitation pulse. The exponential term describes the envelope of the FID. To estimate M_0, we consider the initial amplitude of the signal (i.e., $\mathrm{M}(t=0)$); equation 4 states that the initial amplitude equals the product of M_0 and $m_\perp$. Therefore, if a reliable M_0 is to be produced given this toy problem (where $\mathrm{M}_0 = 1$), the result of the excitation modeling ($m_\perp$) must be consistent with the initial amplitude of the signal ($\mathrm{M}(t=0)$); i.e., $m_\perp = \mathrm{M}(t=0)$ if $\mathrm{M}_0 = 1$. Note that the surface NMR inverse problem is effectively the same as solving this toy problem at every location in the subsurface simultaneously, with the addition of other weighting factors. The toy problem is selected in place of the full surface NMR forward problem to isolate the role that excitation modeling and RDP effects play in estimating the water content.

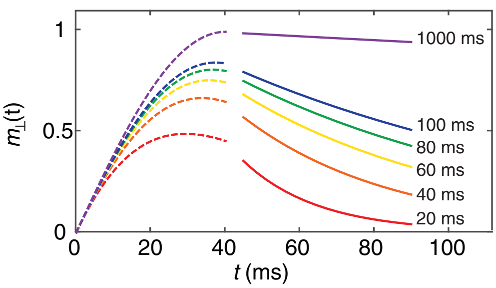

Figure 2. The growth (dashed) and subsequent decay (solid) of the transverse magnetization produced by a 40 ms on-resonance pulse. Colors correspond to a particular T_2^* magnitude. The $T_2 \sim = T_2^*$ regime is present (i.e., $T_2^* = T_2 = T_1$ in this case), and $\mathrm{B}_1 = 1.47\mathrm{e}-7$ T.

Relaxation during the pulse

The relaxation processes that control the time dependence of the FID also take place during the excitation pulse. This can lead to challenges ensuring that the modeled $m_\perp$ is consistent with the initial amplitude of the signal ($\mathrm{M}(t=0)$). To demonstrate why this can be challenging, we return to the previously mentioned toy problem, where Figure 2 illustrates the growth (dashed lines) and subsequent decay (solid lines) of the transverse magnetization produced by a 40 ms on-resonance pulse (a standard pulse in surface NMR where $\omega_0 = \omega_t$) for varying magnitudes of T_2^* (in the $T_2 \sim = T_2^*$ regime). Each profile color corresponds to a different T_2^*. The B_1 in each case is equal to 1.47e-7 T and $T_1 = T_2$. The initial condition in each case is a unit magnetization at equilibrium. All excitation and FID modeling is performed by solving equation 1 using a fourth-order Runge-Kutta solver. Figure 2 shows that as T_2^* decreases so does the magnitude of the transverse component at the end of the pulse ($t = 40$ ms). As a result, the decays in each case have very different amplitudes. The difficulty is that we must be able to reproduce the same M_0 estimate from each of these decays because they all correspond to a unit magnitude ($\mathrm{M}_0 = 1$). To ensure reliable M_0 estimates in the presence of RDP, a protocol is needed that when applied to this toy problem can ensure that the modeled $m_\perp$ is equal to the initial amplitude of the signal ($\mathrm{M}(t=0)$). Otherwise, RDP can bias the estimated water contents (Walbrecker et al., 2009).

To more rigorously demonstrate how RDP affects the ability of the excitation pulse to generate a transverse magnetization, consider Figure 3, which illustrates the final transverse magnetization produced over a range of B_1 for varying magnitudes of RDP. The profile colors correspond to a particular T_2^* magnitude; the investigated T_2^* are 40, 60, 80, 100, 200, 400, and 600 ms (red to purple). Each panel considers almost three orders of magnitude of B_1; it is important to consider such a large B_1 range because the B_1 in surface NMR is extremely heterogeneous. Small and large B_1 are representative of locations far from and close to the transmit coil, respectively. Each m_x and m_y value in the profiles is formed by solving equation 1 given an initial condition described by a unit

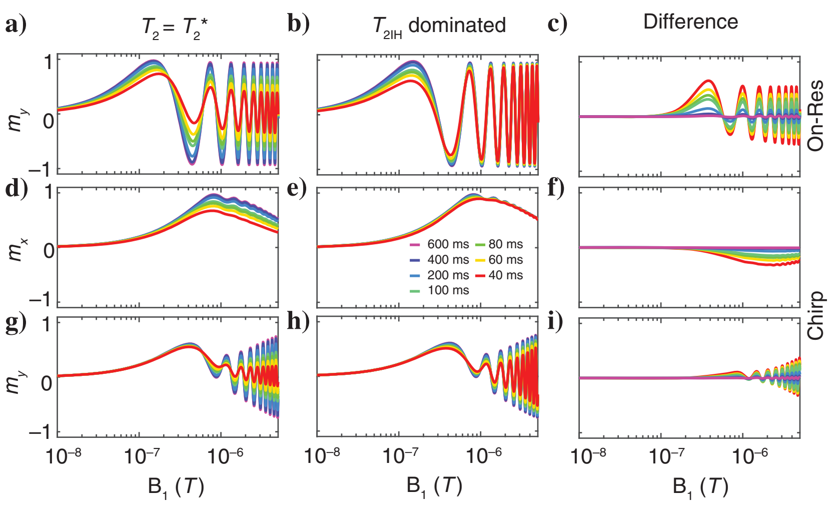

Figure 3. The final transverse magnetization produced over a range of B_1 for varying magnitudes of RDP. The top row corresponds to a 40 ms on-resonance pulse (only the m_y-component is shown as $m_x = 0$ in this case). The bottom two rows correspond to the m_x- and m_y-components produced by a chirp pulse described by a 60 ms linear 100 Hz frequency sweep. The left, center, and right columns correspond to the $T_2 \sim = T_2^*$ regime, the $T_{2\mathrm{IH}}$-dominated regime, and the difference between the two regimes, respectively. The profile colors correspond to a particular T_2^*. $T_1 = T_2 = T_2^*$ in the left column, whereas $T_1 = T_2 = 750$ ms in the center column.

magnetization at equilibrium, a single magnitude of B_1, a single T_2^*, and a $\mathbf{B}_{\mathbf{eff}}(t)$ waveform described by the chosen excitation pulse. Note that a particular T_2^* value can potentially lead to varying magnitudes of RDP depending on which T_2^* regime is present (e.g., $T_2 \sim = T_2^*$ versus $T_{2\mathrm{IH}}$ dominated). Figure 3 considers the $T_2 \sim = T_2^*$ regime (left column) and the $T_{2\mathrm{IH}}$ dominated regime (middle column). The right column shows the difference between the m_x and m_y values produced in the two regimes. In the $T_2 \sim = T_2^*$ regime, T_2^* may be substituted directly into equation 1 in place of T_2. This corresponds to an assumption that B_0 is homogeneous. In the $T_{2\mathrm{IH}}$ dominated regime, where T_2^* is controlled by B_0 inhomogeneity T_2^* cannot be directly substituted in place of T_2. Instead, $m_\perp$ is formed by the weighted sum

$$m_\perp = \sum_i A_i m_{\perp,i}, \tag{5}$$

where $m_{\perp,i}$ corresponds to the transverse magnetization produced for the ith Larmor frequency and A_i corresponds to the relative abundance of the ith Larmor frequency. Each $m_{\perp,i}$ is determined by solving equation 1 given its specific $\mathbf{B}_{\mathbf{eff}}$. Each Larmor frequency will have a different $\mathbf{B}_{\mathbf{eff}}$ because the z-component in equation 2 will differ. The destructive interference that occurs during the summation in equation 5 is representative of the signal loss due to dephasing in the inhomogeneous B_0 field. The coefficients A_i are determined from the magnitude of $T_{2\mathrm{IH}}$,

$$A_i(\Delta\omega_i) = \frac{C_0}{(\Delta\omega_i)^2 + \left(\frac{1}{T_{2\mathrm{IH}}}\right)^2}, \tag{6}$$

where $\Delta\omega_i$ is the offset between the transmit and the ith Larmor frequency. The term C_0 is a scalar used to normalize the area under the $A(\Delta\omega)$ curve; the $A(\Delta\omega)$ curve is the representative of the B_0 distribution. Equation 6 corresponds to a Lorentzian B_0 distrbution. The Lorentizian B_0 distribution follows from an assumption that signal loss due to B_0 inhomogeneity is well-described by a decaying exponential (Chen et al., 2005). Further discussion about alternate shapes of the B_0 distribution is given in the "Discussion" section. In the $T_{2\mathrm{IH}}$-dominated regime, the magnitude of $T_{2\mathrm{IH}}$ can be estimated from equation 3 using the observed T_2^* value and an estimate of T_2 (where T_2 is large). In the $T_{2\mathrm{IH}}$-dominated examples in Figure 3, $T_2 = 750$ ms. Note that solving equation 1 also requires T_1 to be specified. In practice, T_1 typically ranges from approximately 1 to 3 times the magnitude of T_2 (Kleinberg and Farooqui, 1993). The modeling in Figure 3 uses $T_1 = T_2$; i.e., $T_2^* = T_2 = T_1$ in the left column, and $T_2 = T_1 = 750$ ms in the middle column.

The top row of Figure 3 shows the transverse magnetization produced by a 40 ms on-resonance pulse. Only the m_y-component is shown for the on-resonance pulse because the m_x-component was equal to zero. Note that in the $T_{2\mathrm{IH}}$-dominated regime, for all $\omega_{0,i} \neq \omega_t$ the pulse is not technically "on-resonance" but it rather causes off-resonance excitation. However, we will refer to this pulse type as on-resonance given that it represents an attempt to perform on-resonance excitation. For the $T_2 \sim = T_2^*$ case (Figure 3a), the profiles all exhibit similar shapes, with the primary effect of RDP being to reduce the peak amplitudes. The oscillation between positive and negative values at a large B_1 is due to the on-resonance pulse producing large flip angles at these B_1 strengths (e.g., peak positive and negative values occur for rotation angles of $\pi/2 + 2\pi n$ and $3\pi/2 + 2\pi n$, where $n = 0, 1, 2, 3, \ldots$). The position of the main peak at $B_1 \sim 1.5\mathrm{e}-7\mathrm{T}$ is also observed to show a small dependence on the T_2^* value. For the $T_{2\mathrm{IH}}$-dominated case (Figure 3b), the profiles show less variation with T_2^*. At a small B_1, the magnitude of the main peak at $B_1 \sim 1.5\mathrm{e}-7$ T reduces with T_2^*, although its position does not appear to shift to a larger B_1 as was observed in Figure 3a. At a large B_1, the profiles show little dependence on T_2^*, tracking one another closely. The profiles likely track one another closely because the $\mathbf{B}_{\mathbf{eff}}$ axes for different Larmor frequencies are quite similar in the large B_1 limit (i.e., the z-component is much smaller than the x-component in equation 2 at a large B_1 for the small offsets). Figure 3c compares transverse magnetization produced in each regime (the profiles in Figure 3c are equal to the profiles in Figure 3a minus the profiles in Figure 3b). For the smallest investigated T_2^* (red), the two regimes lead to significantly different transverse magnetizations; the difference profiles reach values almost as large as the m_y profiles in each regime. For larger T_2^* values, the profiles become similar (noted by the difference approaching zero).

An additional factor that may impact the magnitude of RDP is the current waveform describing the excitation pulse (Hajduk et al., 1993). In the previous on-resonance pulse example, the transmit frequency is fixed and $\mathbf{B}_{\mathbf{eff}}$ (equation 2) is constant throughout the pulse. However, for many types of pulses, this is not the case. For example, adiabatic pulses, which are the subject of recent surface NMR research (Grunewald et al., 2016), vary the transmit frequency throughout the pulse resulting in a dynamic $\mathbf{B}_{\mathbf{eff}}$ orientation. As a result, the trajectory of the magnetization is very different than the trajectory during an on-resonance pulse, potentially leading to different sensitivities to RDP. Further detail about adiabatic pulses can be found in Tannus and Garwood (1997). The bottom two rows of Figure 3 illustrate the transverse magnetization produced by an example adiabatic pulse that begins with the transmit frequency 100 Hz off-resonance and sweeps linearly toward the Larmor frequency in 60 ms, referred to in the following as a chirp pulse. The B_1 amplitude during the chirp pulse is coupled to the instantaneous offset via a coil response described by a Lorentzian whose width corresponds to a coil quality factor of 10 and a center frequency of 2000 Hz. This is done to approximate surface NMR transmit conditions, in which the transmit coils are tuned and will result in similar B_1 modulation during the adiabatic pulse. This particular chirp pulse is chosen for its simplicity and its similarity to the adiabatic pulse previously demonstrated in a surface NMR field test by Grunewald et al. (2016). This pulse is not optimized for surface NMR conditions; it merely functions to contrast the behavior of an adiabatic pulse against the standard on-resonance case. The middle and bottom rows illustrate the m_x- and m_y-components of the transverse magnetization following the chirp pulse, respectively. Consider first the m_x-component (middle row of Figure 3). The m_x profiles are described by a single broad peak containing only positive values. This is a consequence of the adiabatic pulse exhibiting reduced sensitivity to B_1 heterogeneity (Tannus and Garwood, 1997). For the $T_2 \sim = T_2^*$ case (Figure 3d), the magnitude of the main peak reduces for smaller values of T_2^*. For the $T_{2\mathrm{IH}}$-dominated case (Figure 3e), the profiles show little dependence on T_2^*, tracking one another closely over the full range of investigated B_1. Adiabatic pulses tend to display reduced sensitivity to B_0 heterogeneity, effectively allowing the chirp pulse to improve coherence between the different Larmor frequencies (Tannus and Garwood, 1997), which causes the profiles in Figure 3e to appear very similar. Comparing the m_x profiles for each regime (Figure 3f) indicates that RDP during the chirp pulse is stronger in the $T_2 \sim = T_2^*$ regime compared with the T_{2IH}-dominated regime. The m_y-component following the chirp pulse (bottom row) is described by an initial peak at a small B_1 followed by strong oscillations at a large B_1. The oscillations are not a result of modeling instability, but they rather are a consequence of the adiabatic condition not being well-satisfied at a large B_1 given the initial 100 Hz offset of the investigated chirp pulse (Grunewald et al., 2016). Larger initial offsets will reduce the magnitude of the oscillation and can help extend the right side of the main peak in the m_x profile to larger B_1. In the $T_2 \sim = T_2^*$ case (Figure 3g), the m_y dependence on T_2^* is similar to that shown by the m_x-component (Figure 3d). The final m_y-component decreases for smaller T_2^*, with the reduction being most significant at a large B_1. For the T_{2IH}-dominated case (Figure 3h), the m_y-component shows less T_2^* dependence, with a small reduction at a large B_1. The difference in the m_y profiles (Figure 3i) is minimal at a small B_1, but it begins to strongly oscillate at a large B_1. As T_2^* increases in magnitude, the difference between the two regimes approaches zero.

To summarize, the impact of RDP on the final transverse magnetization displays a complex dependence on B_1, the magnitude of T_2^*, the T_2^* regime, and the excitation pulse type. Given hardware advancements allowing the measurement of faster relaxation times (where RDP is strongest) and a growing interest in the use of alternative excitation schemes, a robust approach providing reliable M_0 estimates in the presence of RDP for arbitrary excitation pulse types is required.

Methods to account for RDP effects

Two approaches have been used in surface NMR to deal with RDP. The first approach, EEP, effectively assumes that RDP is negligible; a reasonable assumption in the $\tau \ll T_2^*$, T_1 limit. In this case, the excitation modeling neglects the relaxation terms in equation 1, and the initial amplitude of the signal is equal to the amplitude of the decay immediately following the end of the pulse. In practice, the initial amplitude cannot be observed directly because measurement of the decay begins a finite time after the end of the pulse. This delay, called the dead time t_{dead}, is necessary because the ramp down of the current in the transmit coil is not instantaneous and the instrument must be switched from transmit mode to receive mode. The characteristics of the filters used in data processing also contribute to the dead time. Therefore, to estimate the initial amplitude, the observed decay must be extrapolated back in time to the end of the pulse. This is accomplished by first determining the T_2^* that best describes the observed decay and then using this T_2^* estimate to extrapolate the decay to $t = 0$, where $t = 0$ at the end of the excitation pulse and the first time sample of the measured decay occurs at $t = t_{dead}$. If this approach is reliable, the value of the extrapolated decay at the end of the pulse should be closely reproduced by excitation modeling that neglects RDP; any discrepancy between the estimated initial amplitude and the excitation modeling may bias the final water content estimate (Walbrecker et al., 2009).

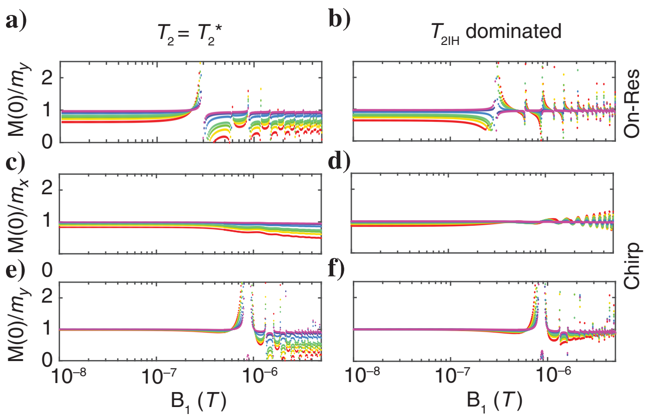

Figure 4. The accuracy of the extrapolation to end-pulse (EEP) approach for an on-resonance (top row) and chirp pulse (bottom two rows) over a range of B_1 for varying magnitudes of RDP. The left and right columns correspond to the $T_2 \sim = T_2^*$ regime and the T_{2IH}-dominated regime, respectively. The profile colors correspond to a particular T_2^* magnitude; the profile colors are the same as in Figure 3. The T_1 and T_2 in each regime are the same as in Figure 3. The initial amplitude M(0) is calculated at the end of the pulse. Ratios close to one correspond to regions where the M_0 estimates would be accurate.

Figure 4 illustrates the accuracy of the EEP approach for the same two pulses investigated in Figure 3; the top and bottom two rows correspond to the on-resonance and chirp pulse, respectively. The left and right columns correspond to the $T_2 \sim = T_2^*$ regime and the T_{2IH} dominated regime, respectively. The colors of each profile correspond to a particular T_2^* value; the T_2^* values in Figure 4 are the same as in Figure 3. The B_1 range is also the same as in Figure 3. Each point in the profiles corresponds to the ratio of the initial amplitude of the decay (estimated by extrapolation to the end of the pulse) and the expected m_x or m_y value determined by solving equation 1 without the relaxation terms present. This ratio represents the accuracy of the EEP approach. Reliable performance corresponds to a ratio of one, whereas the magnitude of the deviation from one indicates how biased the M_0 estimate will be. To form an initial amplitude estimate, an FID experiment is simulated. To simulate an FID experiment equation 1 (given the appropriate B_1, T_2^*, T_2^* regime, excitation pulse and an initial condition described by a unit magnetization at equilibrium) is solved from $t = 0$ (start of the pulse) until $t = \tau + 150$ ms (150 ms after the end of the pulse). Note that no B_1 field is present from $t = \tau$ to $t = \tau + 150$ ms. The synthetic FID is formed by sampling the transverse components (m_x and m_y) of the magnetization from $t = \tau + t_{dead}$ until $t = \tau + 150$ ms. A dead time of 5 ms is used in all cases. A monoexponential decay is fit to the synthetic FID and used to extrapolate back to the end of the pulse to form the initial amplitude estimate. Consider first the 40 ms on-resonance pulse case (top row of Figure 4). At a small $B_1 (B_1 < \sim 3e-7$ T) the $T_2 \sim = T_2^*$ and T_{2IH}-dominated regimes exhibit ratios less than one, where the magnitude of the deviation from one increases as T_2^* decreases. Producing ratios less than one is equivalent to underestimating M_0 and would ultimately lead to underestimated water contents. As T_2^* increases the ratios approaches one. At larger $B_1 (B_1 > \sim 3e-7$ T), in the $T_2 \sim = T_2^*$ regime the ratios are again consistently less than one, with the bias increasing as T_2^* decreases. Alternatively, at large B_1 the EEP approach consistently produces ratios close to one in the T_{2IH} dominated regime. Note that the discontinuities in the profiles occur at the locations of the zero crossings in the on-resonance m_y profiles in Figure 3.

The bottom two rows of Figure 4 illustrate the performance of the EEP approach for the chirp pulse (the middle and bottom rows illustrate the m_x and m_y ratios, respectively). The profiles are formed in the same manner as in the top row. Consider first the m_x ratio. In this case, both regimes show similar behavior at $B_1 < \sim 3e-7$ T, where the ratio is close to one (small underestimates as T_2^* decreases). At a large B_1, the two regimes show differing behavior. In the $T_2 \sim = T_2^*$ regime (Figure 4c), as T_2^* decreases the magnitude of the bias increases (the ratio deviates further from one) and M_0 would be consistently underestimated. Alternatively, at a large B_1 in the T_{2IH} dominated regime, the profiles (Figure 4d) are centered at approximately 1, and instead show an oscillation that increases in magnitude as T_2^* decreases. For the m_y-component (bottom row), the ratios are close to one at a small B_1 in both regimes, but they begin to exhibit behavior similar to the on-resonance case at a large $B_1 (B_1 > \sim 8e-7$ T). At a large B_1 in the $T_2 \sim = T_2^*$ regime (Figure 4e), as T_2^* decreases, the ratios are consistently less than one (with the bias increasing as T_2^* decreases). For the T_{2IH}-dominated regime (Figure 4f), the ratios are consistently much closer to one, with a small bias present for the smallest T_2^*. Note that in both regimes, the ratios deviate significantly from one at $B_1 \sim = 8e-7$ T, which correspond to the first minima after the main peak in the m_y profiles in the bottom row of Figure 3.

To improve upon the EEP approach, Weichman et al. (2000) and Walbrecker et al. (2009) suggest that the EMP approach may be used, in which the initial amplitude is now estimated by extrapolating the observed decay to the middle of the pulse. In this case, $t = 0$ occurs at the pulse midpoint and the first time sample of the measured decay occurs at $t = \tau/2 + t_{\mathrm{dead}}$, where τ is the pulse duration. The reasoning behind this approach is that shifting the time zero from the end of the pulse to the midpoint allows the extrapolated decay to reach a value that more closely approximates modeling that determines $m_\perp$ by solving equation 1 with no relaxation terms present. The EMP approach presents a simple, easy-to-implement scheme to account for RDP; it only requires adjusting the time when the initial amplitude is estimated, and it does not need alterations to the modeling of $m_\perp$. To demonstrate the performance of the EMP approach, Figure 5 illustrates the ratio of the initial amplitude (estimated by extrapolating a synthetic FID to the middle of the pulse) and the $m_\perp$ value produced by solving equation 1 without relaxation terms. The same conditions as in Figure 3 are investigated. Consider first the 40 ms on-resonance pulse case (top row). In both regimes, the ratio is close to one at a small B_1 ($< \sim 2e-7$ T) for all investigated T_2^*. In the large T_2^* cases (purple and blue), the ratio is close to one even at a large B_1. However, for smaller T_2^* values, the ratio deviates from one with the magnitude of the bias increasing for smaller values of T_2^*. The bias is also different in the two regimes; for the $T_2 \sim = T_2^*$ regime (Figure 5a) the ratio is less than one at a large B_1, whereas the ratio is greater than one in the T_{2IH}-dominated regime (Figure 5b). Note that the biases observed in the top row of Figure 5 persist to longer T_2^* and are larger than those observed in Walbrecker et al. (2009), who also consider RDP during a 40 ms on-resonance pulse. For example, for $T_2^* = 100$ ms (light green profiles) the ratios at large B_1 in the $T_2 \sim = T_2^*$ and T_{2IH} dominated regime are centered approximately 0.8 and 1.2, respectively. Further discussion about the source of the discrepancy between the results shown in the top row of Figure 5 and Walbrecker et al. (2009) is given in the "Discussion" section. Briefly, the differences originate from the larger B_1 range considered in Figure 5 and a difference in the T_1 values used in the modeling. Comparing the top rows of Figures 4 and 5 indicates that the EMP approach greatly improves performance for the 40 ms on-resonance pulse at small $B_1 (B_1 < \sim 2e-7$ T). At a larger B_1, the EMP approach performs slightly better than the EEP approach in the $T_2 \sim = T_2^*$ regime, whereas the EEP approach provides better results in the T_{2IH}-dominated regime at strong B_1 for the on-resonance pulse.

The EMP approach was originally proposed in the context of an on-resonance excitation scheme. To test its performance for an alternative pulse type, the bottom two rows of Figure 5 illustrate the performance of the EMP approach for the same chirp pulse and conditions considered in Figure 3. The middle and bottom rows of Figure 5 illustrate the performance for the m_x- and m_y-components, respectively. Consider first the m_x-component. In this case, the ratio deviates from one considerably for both regimes over the full range of investigated B_1, with the magnitude of the bias increasing as T_2^* decreases. For the $T_2 \sim = T_2^*$ regime, the bias is reduced at a stronger B_1 (the profiles converge toward 1). Alternatively, the bias remains at a strong B_1 for the T_{2IH} dominated regime. Note that the bias is significant even at moderate T_2^* values (e.g., the ratio is approximately 1.3 for $T_2^* = 100$ ms (light green)). The m_y-components (Figure 5e and 5f) show similar behavior to m_x, with the ratio significantly deviating from one at small B_1. Again the magnitude of the bias increases with decreasing T_2^*. At stronger $B_1 (> \sim 8e-7$ T), the m_y ratio shows similar behavior as the on-resonance (Figure 5a and 5b), where the ratio is less than one in the $T_2 \sim = T_2^*$ regime and greater than one in the T_{2IH}-dominated regime with the magnitude of the bias increasing for decreasing T_2^*. Comparing the bottom two rows of Figures 4 and 5 indicates that the EEP approach provides improved performance compared with the EMP approach for this example chirp pulse. However, this does not indicate that all adiabatic pulses are better suited to the EEP approach.

To demonstrate that alternative adiabatic pulses may display differing behavior to that shown by the chirp pulse, Figure 6 contrasts the performance of the EEP and EMP approaches for an adiabatic pulse whose frequency sweep is described by a hyperbolic tangent function (referred to in the following as a tanh pulse). This particular tanh

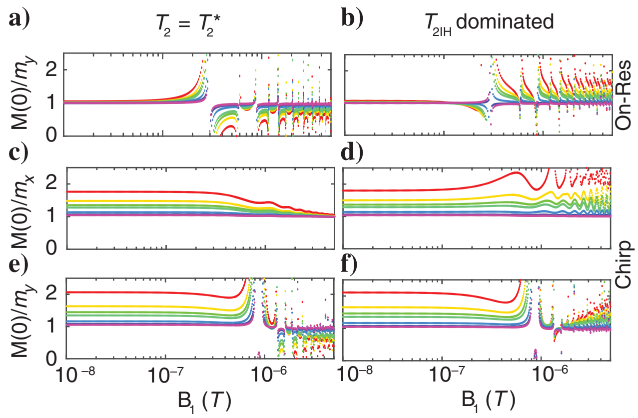

Figure 5. The accuracy of the extrapolation to mid-pulse (EMP) approach for an on-resonance (top row) and chirp pulse (bottom two rows) over a range of B_1 for varying magnitudes of RDP. The left and right columns correspond to the $T_2 \sim = T_2^*$ regime and the T_{2IH}-dominated regime, respectively. The profile colors correspond to a particular T_2^* magnitude; the profile colors are the same as in Figure 3. The T_1 and T_2 in each regime are the same as in Figure 3. The initial amplitude M(0) is calculated at the middle of the pulse. Ratios close to one correspond to regions where M_0 estimates would be accurate.

pulse is 60 ms in duration, begins 250 Hz off-resonance, and has $\eta = 5$; i.e., the offset at each moment in the pulse is described by $\Delta\omega(t) = 2\pi \times 250\ \mathrm{Hz}(1 - \tanh(\eta t/\tau)/\tanh(\eta))$. The B_1 amplitude during the tanh pulse is modulated using the same coil response as the previous chirp pulse. The conditions (B_1, T_2^*, T_1) in Figure 6 are the same as in Figure 3. The top (Figure 6a–6d) and bottom (Figure 6e–6h) cluster of subplots correspond to the ratios of the initial amplitude estimates and the modeled m_x- and m_y-components, respectively. Each row corresponds to the results produced by either the EEP or EMP approach (stated at the right of each row). Consider first the m_x-component (Figure 6a–6d). In this case, the EMP approach performs better in the $T_2 \sim = T_2^*$ regime (Figure 6a and 6c), whereas the EEP and EMP approach only provide reliable performance over a limited B_1 range in the $T_{2\mathrm{IH}}$-dominated regime (Figure 6b and 6d). Given that this tanh pulse only produces appreciable m_x-components at $B_1 > \sim 3e-7$ T (not shown, but the tanh m_x profile is similar to Figure 3d), the EEP approach is likely to produce more reliable results in the $T_{2\mathrm{IH}}$-dominated regime. For the m_y-components (Figure 6e–6h), the EEP and EMP approaches produce ratios that deviate from one at a small B_1; with a bias toward ratios of less than one and greater than one for the EEP and EMP approaches, respectively. At a larger B_1, the accuracy of the EEP and EMP approaches for the m_y-component is similar to that shown by the on-resonance pulse (the top rows of Figures 4 and 5). In the $T_2 \sim = T_2^*$ regime (Figure 6e and 6g), the ratios are typically less than one with the magnitude of the bias increasing as T_2^* decreases for the EEP and EMP approaches. For the $T_{2\mathrm{IH}}$-dominated regime at a large B_1 (Figure 6f and 6g), the EEP approach consistently produces ratios close to one, whereas the EMP approach produces ratios greater than one, with the magnitude of the bias increasing for decreasing T_2^*. Overall, the optimal time at which to calculate the initial amplitude for the tanh pulse (the end of the pulse versus middle of the pulse versus some alternative time) depends strongly on the B_1 range, the T_2^* scenario, and it may differ for the m_x- and m_y-component.

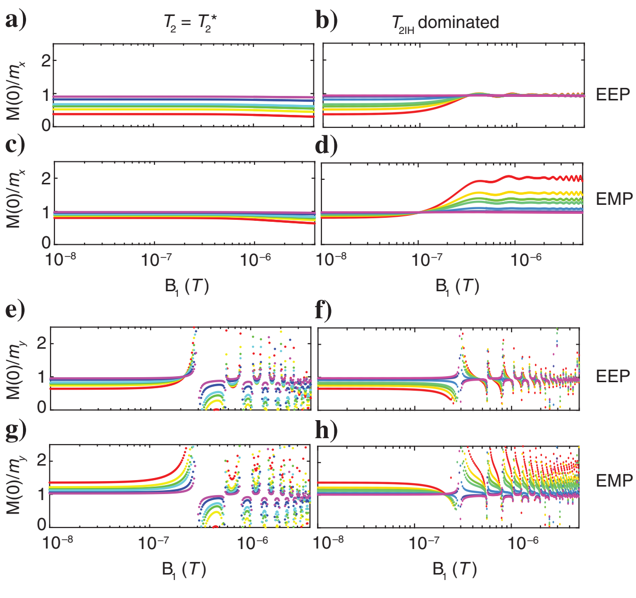

Figure 6. The accuracy of the EEP and EMP approaches for an adiabatic pulse described by a frequency sweep controlled by a hyperbolic tangent function (details are given in the text) over a range of B_1 for varying magnitudes of RDP. The left and right columns correspond to the $T_2 \sim = T_2^*$ regime and the $T_{2\mathrm{IH}}$-dominated regime, respectively. The upper (a-d) and lower (e-h) clusters correspond to the m_x- and m_y-components, respectively. Each row corresponds to ratios produced using either the EEP or EMP approach (indicated at the right of each column). The profile colors correspond to a particular T_2^* magnitude; the profile colors are the same as in Figure 3. The T_1 and T_2 in each regime are the same as in Figure 3. Ratios close to one correspond to regions where the M_0 estimates would be accurate.

Figures 4, 5, and 6 demonstrate that surface NMR excitation modeling schemes that solve the Bloch equation without relaxation terms present (and attempt to compensate for RDP by adjusting the time at which the initial amplitude is calculated) may produce biased M_0 estimates in certain conditions. The reliability of these approaches depend strongly upon B_1, T_2^*, the T_2^* scenario, the excitation pulse waveform, and selection of an appropriate time zero. Some pulses may even require different time zeros depending on which T_2^* scenario is present or whether we are calculating the initial amplitude of the m_x- or m_y-component (e.g., Figure 6). Furthermore, these types of schemes (EEP and EMP) can also introduce different types of M_0 biases (over- versus underestimation) depending on which T_2^* scenario is present. This illustrates the need for a flexible approach to account for RDP that can handle an arbitrary excitation pulse, perform reliably in all T_2^* scenarios, and can extend the range of B_1 and T_2^* where accurate results can be produced.

UPDATING THE FORWARD MODEL TO INCLUDE RDP

We propose a data-driven scheme to accommodate for RDP in which relaxation time estimates are used to update the excitation modeling to directly include RDP effects; this scheme is referred to as the MRDP approach. We hypothesize that such an approach will improve the excitation modeling's ability to robustly reproduce the initial amplitude for a broader range of conditions. For the MRDP scheme, the initial amplitude is the initial value of the observed decay; no extrapolation is performed. Instead, the value of $m_\perp$ will be calculated by solving the Bloch equation until the end of the dead time (i.e., from $t = 0$ [the start of pulse] to $t = \tau + t_{\mathrm{dead}}$ [the end of the dead time]). Note that no B_1 is present from $t = \tau$ to $t = \tau + t_{\mathrm{dead}}$. A potential advantage of determining $m_\perp$ at the end of the dead time is that it may help facilitate easier handling of any nonexponential behavior of the observed decays at early times (Grunewald and Knight, 2012). When modeling $m_\perp$ for the MRDP scheme, equation 1 will be solved with appropriately weighted relaxation terms present. That is, the magnitude of the relaxation terms in the Bloch equation will be based on the value of T_2^* fit to the observed decay. This requires an assumption about which T_2^* scenario is present. Given that little information is typically available to constrain this assumption, it is advisable to treat the data as if both end-member scenarios are present (i.e., treat the data as if the $T_2 \sim = T_2^*$ regime is present and then again as if the $T_{2\mathrm{IH}}$-dominated regime is present). This provides us the opportunity to gain insight into uncertainty in the estimated water contents that stems from an inability to uniquely determine the correct modeling scenario. Note that T_1, which is poorly constrained given only FID measurements, must also be estimated in the MRDP approach; a discussion of the MRDP approach's sensitivity to the T_1 estimate is given later in this section.

To illustrate the potential advantages and limitations of the MRDP approach, Figures 7 and 8 illustrate the accuracy of the MRDP scheme for the same conditions investigated in Figure 3. Figures 7 and 8 show the 40 ms on-resonance pulse case and chirp pulse case, respectively. The rows in Figure 7 correspond to the T_2^* scenario used to forward model the synthetic data (the top and bottom rows correspond to the $T_2 \sim = T_2^*$ and $T_{2\mathrm{IH}}$-dominated regimes, respectively). The left and right columns correspond to the T_2^* scenario used by the MRDP scheme (the left and right columns correspond to the $T_2 \sim = T_2^*$ and $T_{2\mathrm{IH}}$-dominated regimes, respectively). Therefore, Figure 7a and 7d represents cases in which the MRDP scheme is given the correct modeling scenario, whereas Figure 7b and 7c represents the case in which the MRDP scheme uses the wrong modeling scenario. Figure 7b and 7c effectively represents worst-case scenarios. Figure 7a and 7d shows that given the correct modeling scenario, the MRDP scheme can reliably estimate M_0 for the 40 ms on-resonance pulse over the full range of B_1. Although some errors are observed in Figure 7d near the location of the zero crossings in the m_y profiles in Figure 3b, the ratios are consistently close to one for all T_2^*. Note that Figure 7a and 7d represents the best-case scenario, in which the modeling was also given the correct value of T_1. Further discussion regarding sensitivity of the MRDP approach to the T_1 estimate is given later in this section. Figure 7b and 7c shows that the MRDP scheme produces biased M_0 estimates when the incorrect modeling scenario is used. The magnitude of the bias increases as T_2^* decreases. In the $T_2 \sim = T_2^*$ regime (Figure 7b), choosing an incorrect modeling scenario will result in underestimated M_0 at large B_1. Alternatively, in the $T_{2\mathrm{IH}}$-dominated regime (Figure 7c) choosing an incorrect modeling scenario will degrade performance over the full range of B_1, producing ratios of less than one and greater than one at small and large B_1, respectively. The biases present at a large B_1 in Figure 7b and 7c are similar in magnitude to the top row of Figure 5 (the EMP approach).

Figure 8 illustrates the performance of the MRDP scheme for the same chirp pulse considered in Figure 3. The m_x- and m_y-components are shown in the top two and bottom two rows, respectively. Similar to Figure 7, each row in Figure 8 corresponds to the T_2^* scenario used to forward model the synthetic data, whereas each column corresponds to the T_2^* scenario used by the MRDP scheme. Consider first the m_x-component. Given the correct modeling scenario (Figure 8a and 8d), the MRDP scheme reliably estimates M_0 over the full investigated B_1 range. Note that this represents the best-case scenario, in which the correct T_1 value is used by the MRDP scheme. Given the incorrect modeling scenario (Figure 8b and 8c), the MRDP scheme performs well at small B_1 but produces a biased result at stronger B_1. The magnitude of the bias again increases with decreasing T_2^*. In the $T_2 \sim = T_2^*$ regime (Figure 8b), selection of the incorrect modeling scenario results in ratios less than one at large B_1. The magnitude of the bias at a large B_1 in Figure 8b is similar in magnitude to that observed in Figure 4c (the EEP approach). Alternatively, in the $T_{2\mathrm{IH}}$-dominated regime selection of the incorrect modeling scenario results in ratios greater than one at large B_1. The bias observed in Figure 8c is much larger than that observed in Figure 4d (the EEP approach). For the m_y-components, the observed behavior is similar to the m_x-components. Given the correct modeling scenario, the MRDP approach can reliably estimate M_0 over the full range of B_1 (Figure 8e and 8h). A small bias toward ratios less than one at a large B_1 is observed in Figure 8h for the smallest T_2^* (red profile). If the wrong modeling scenario is used (Figure 8f and 8g), the initial amplitude is estimated reliably at a small B_1, whereas significant biases are introduced at a large B_1 for small T_2^*, with the magnitude of the bias increasing with decreasing T_2^*. For large T_2^* (blue and purple profiles), the ratio approaches one, indicating that a reliable m_y-component can be estimated even at a large B_1. In the $T_2 \sim = T_2^*$ regime (Figure 8f), selection of the incorrect modeling scenario results in ratios of less than one at a large B_1. The bias at a large B_1 in Figure 8f is larger than that observed in Figure 4e (the

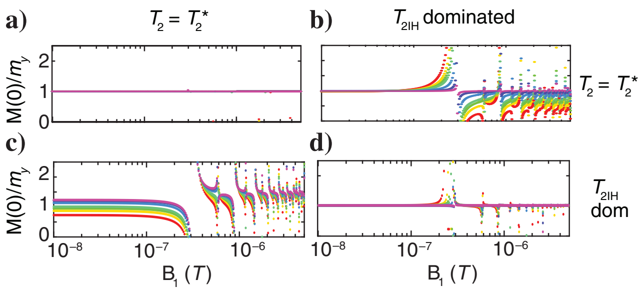

Figure 7. Accuracy of the MRDP approach for a 40 ms on-resonance over a range of B_1 for varying magnitudes of RDP. The top and bottom rows correspond to synthetic FIDs that were produced given the $T_2 \sim = T_2^*$ and the $T_{2\mathrm{IH}}$-dominated regimes, respectively. The left and right columns correspond to MRDP results that assumed that the $T_2 \sim = T_2^*$ and the $T_{2\mathrm{IH}}$-dominated regimes were present, respectively. That is, (a and d) correspond to an MRDP approach that was given the correct regime, whereas (b and c) correspond to an MRDP approach that was given the incorrect regime. In (a and d) the MRDP approach was given the correct T_1 (and T_2 in d). The profile colors correspond to a particular T_2^* magnitude; the profile colors are the same as in Figure 3. The T_1 and T_2 used to produce the synthetic FIDs in each regime are the same as in Figure 3. Ratios close to one correspond to regions where M_0 estimates would be accurate.

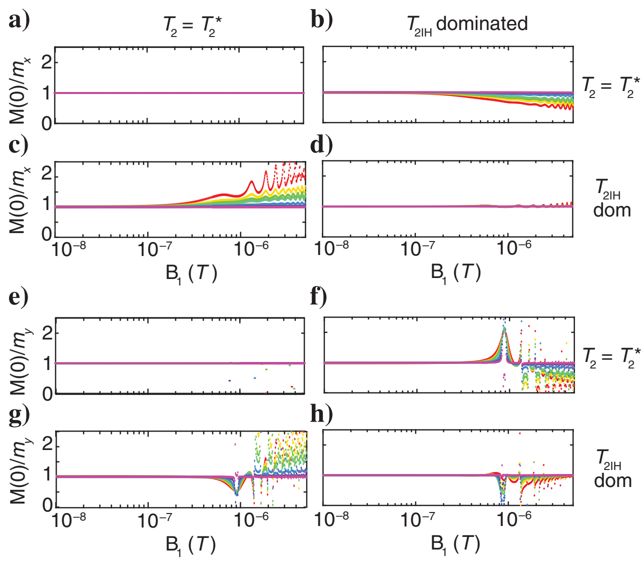

Figure 8. Accuracy of the MRDP approach for a chirp pulse (the same chirp pulse as in Figure 3) over a range of B_1 for varying magnitudes of RDP. The top and bottom rows in each cluster correspond to synthetic FIDs that were produced given the $T_2 \sim = T_2^*$ and the $T_{2\mathrm{IH}}$-dominated regimes, respectively. The top (a-d) and bottom (e-h) clusters correspond to the m_x- and m_y-components, respectively. The left and right columns correspond to MRDP results that assumed the $T_2 \sim = T_2^*$ and the $T_{2\mathrm{IH}}$-dominated regimes were present, respectively. The profile colors correspond to a particular T_2^* magnitude; the profile colors are the same as in Figure 3. In (a, d, e, and h) the MRDP approach was given the correct T_1 (and T_2 in d and h).The T_1 and T_2 used to produce the synthetic FIDs in each regime are the same as in Figure 3. Ratios close to one correspond to regions where M_0 estimates would be accurate.

EEP approach). Alternatively, in the $T_{2\mathrm{IH}}$-dominated regime, selection of the incorrect modeling scenario results in ratios greater than one at a large B_1. The bias observed in Figure 8G is also larger than that observed in Figure 4f (the EEP approach). Overall, Figures 7 and 8 show that if the correct modeling scenario is selected, the range of B_1 and T_2^* where M_0 can be reliably estimated is improved by the MRDP scheme. If an incorrect modeling scenario is selected, the magnitude of the biases is similar or larger than those introduced by the EEP or EMP approaches.

In Figures 7 and 8, when the MRDP approach used the correct T_2^* scenario, it was also given additional information that is typically unavailable (hence why it was referred to as the best-case scenario). For the $T_2 \sim = T_2^*$ case, the MRDP approach was given the correct value of T_1. For the $T_{2\mathrm{IH}}$ dominated case, the MRDP approach was given the correct value of T_2 and T_1. In practice, if only FID measurements are available the T_1 value is unconstrained and must be estimated (T_2 must also be estimated in the $T_{2\mathrm{IH}}$-dominated regime). Figures 9 and 10 illustrate the sensitivity of the MRDP approach to these parameters. Figure 9 illustrates the sensitivity of the MRDP approach to the estimated value of T_1 in the $T_2 \sim = T_2^*$ regime. The top, middle, and bottom rows illustrate the ratio of the initial amplitude and the modeled m_y for a 40 ms on-resonance pulse, m_x for the chirp pulse, and m_y for the chirp pulse (the same chirp pulse as in Figure 3). In each case, synthetic data are forward modeled with $T_2^* = T_2 = 40$ ms. The left and right columns correspond to data forward modeled using T_1 values of 40 ms ($T_1 = \mathrm{T}_2$) and 120 ms ($T_1 = 3\mathrm{T}_2$), respectively. The profile colors correspond to the T_1 value used by the MRDP approach; the investigated T_1 range spans from T_2 to $3T_2$ in steps of $0.25T_2$ (red to purple). The selected T_1 is chosen to span the range of T_1/T_2 ratios typical of reservoir sediments (Kleinberg and Farooqui, 1993). The black dots correspond to the results produced by the EMP (top row) or EEP (bottom two rows) approach given the same synthetic data and serve

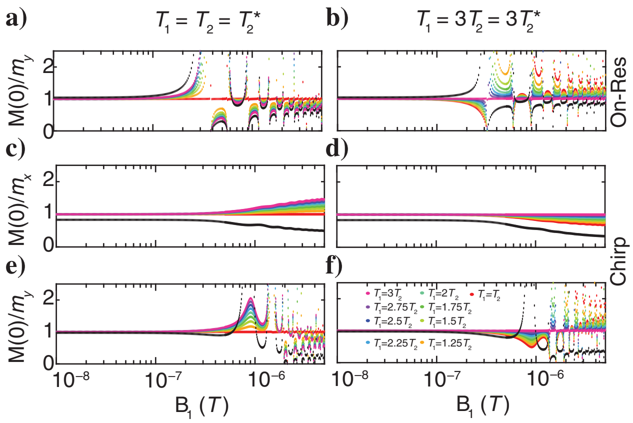

Figure 9. Sensitivity of the MRDP approach to the estimated value of T_1 in the $T_2 \sim = T_2^*$ regime. The top and bottom two rows correspond to the results for a 40 ms on-resonance pulse and a chirp pulse, respectively (same as in Figure 3). The left and right columns correspond to synthetic FIDs that were produced using $T_1 = T_2$ and $T_1 = 3T_2$, respectively; $T_2 = T_2* = 40$ ms in all cases. The profile color corresponds to the estimated T_1 value used in the MRDP approach. T_1 was sampled from T_2 (red) to $3T_2$ (purple) in steps of $0.25T_2$. The black profile in the top row corresponds to the results that would be produced using the EMP approach, whereas the black profiles in the bottom two rows correspond to the results of the EEP approach.

as a reference against which the MRDP results are contrasted. In all cases, as the magnitude of T_1 deviates further from the true T_1 (red to purple in the left column and purple to red in the right column) the bias at large B_1 increases. The estimated T_1 value used in the MRDP approach does not seem to have a significant effect at small B_1 (the ratio is consistently close to one). For the 40 ms on-resonance case (Figure 9a and 9b), the bias at a large B_1 displays similar asymptotic behavior as was seen in the top row of Figure 5. In Figure 9a, the MRDP scheme produces ratios closer to one for all estimated T_1 values compared the EMP approach. In Figure 9b, the MRDP scheme produces a larger bias than the EMP approach when the estimated T_1 is much smaller than the true T_1; the red ($T_1 = T_2$), orange ($T_1 = 1.25T_2$), and yellow ($T_1 = 1.5T_2$) curves are further from one than the black line. For better estimates of T_1, the MRDP approach profiles are closer to one. Consider next the chirp pulse case (the bottom two rows of Figure 9). For the m_x-component (Figure 9c and 9d), all MRDP profiles are closer to one over the full range of B_1 when compared with EEP approach for the $T_1 = T_2$ and $T_1 = 3T_2$ cases. For the m_y-component (Figure 9e and 9f), a similar behavior is observed as for the m_x-component. For all estimated T_1 values, the ratios are consistently closer to one than the black line over the full investigated B_1 range. Only at a small subset of B_1 is the black line closer to one (as the black line crosses through one near the asymptotes). In summary, Figure 9 indicates that the MRDP scheme consistently improves performance compared with the EMP and EEP approaches in the $T_2 \sim = T_2^*$ regime despite the uncertainty about the true value of T_1. Selecting a middle value of T_1 (e.g., $T_1 = 2T_2$, light blue profiles) provides a compromise balancing performance in the $T_1 = T_2$ and $T_1 = 3T_2$ cases. For the on-resonance case, the penalty for underestimating the true T_1 value appears to be more severe than overestimating T_1 (i.e., the biases are larger in Figure 9b than in Figure 9a).

Figure 10 illustrates the sensitivity of the MRDP approach to the estimated values of T_2 and T_1 in the $T_{2\mathrm{IH}}$-dominated regime. The top, middle, and bottom rows illustrate the ratio of the initial amplitude and the modeled m_y for a 40 ms on-resonance pulse, m_x for the chirp pulse, and m_y for the chirp pulse (same chirp pulse as in Figure 3). In each case, synthetic data are forward modeled with $T_2^* = 40$ ms, and $T_1 = T_2$. The left and right columns correspond to synthetic data forward modeled using T_1 values of 100 and 750 ms, respectively. The profile colors correspond to the T_1 and T_2 values used by the MRDP approach; the investigated T_1 and T_2 values are 100, 250, 500, and 750 ms (red to purple). The black dots correspond to the results produced by the EMP (top row) or EEP (bottom two rows) approach given the same synthetic data. The black profiles serve as a reference to contrast the MRDP results. Consider first the on-resonance pulse (top row of Figure 10). For the $T_1 = T_2 =$ 100 ms case (Figure 10a), if T_1 is estimated poorly, the MRDP will introduce larger biases than the EMP approach (the black line is closer to one than the green, blue, and purple lines). For the $T_1 = T_2 = 750$ ms case (Figure 10b), the MRDP approach is less sensitive to the T_1 estimate. The green, blue, and purple profiles produce ratios closer to one over the full B_1 range compared with the EMP approach (black profile). At a large B_1, the poorest T_1 estimate (red profile in Figure 10b) is also able to produce ratios closer to one compared with the EMP approach. Alternatively, at a small B_1, the EMP approach produces ratios closer to one than the red profile. The top row of Figure 10 indicates that the penalty for overestimating T_1 in the

T_{2IH}-dominated regime for the MRDP scheme is more severe than underestimating T_1. For the chirp pulse, the MRDP scheme is more robust given a poor T_1 estimate. For the m_x-component (Figure 10c and 10d) and the m_y-component (Figure 10e and 10f), even if T_1 is estimated poorly, the ratios are consistently closer to one compared with the EEP approach over the full range of investigated B_1 (for the $T_1 = T_2 = 100$ ms and $T_1 = T_2 = 750$ ms cases). For the m_y-component in the $T_1 = T_2 = 750$ ms case (Figure 10f), the poorest T_1 estimate (red profile) produces larger biases than the EEP approach at a large B_1. In summary, Figure 10 indicates that the MRDP approach can improve performance compared with the EEP pulse approach in the T_{2IH}-dominated regime for the chirp pulse even for an incorrect T_1 estimate. For the on-resonance case, T_1 and T_2 must be more accurately estimated to ensure improved performance compared with the EMP approach. Selecting a middle value of T_1 and T_2 (e.g., $T_1 = T_2 = 250$ ms, green profiles) provides good performance in each case.

DISCUSSION

The two approaches previously applied in surface NMR to deal with RDP (the EEP and EMP approaches) involve excitation modeling that neglects RDP, instead attempting to account for RDP by adjusting the time at which the initial amplitude of the signal is calculated. The advantage of these approaches is that they are easy to implement and do not require the excitation modeling to be updated based on the current best estimate of T_2^* (which is equivalent to not requiring the kernel to be updated each iteration in the surface NMR inversion). However, Figures 4, 5, and 6 demonstrate that these approaches struggle to capture the complex dependence of RDP on B_1, T_2^*, the T_2^* scenario, and the excitation pulse type. The EEP and EMP approaches can produce reliable M_0 estimates provided that the time at which the initial amplitude is estimated is appropriate for the particular conditions present (i.e., B_1, T_2^*, T_2^* regime, and the excitation pulse type). A shortcoming of the EEP and EMP approaches stems from the fact that it is difficult to ensure reliable performance over a broad range of B_1, T_2^*, and in all T_2^* regimes. For example, while an on-resonance pulse is better suited to the EMP approach compared with the EEP approach, the EMP approach still produces significant biases at a large B_1 for $T_2^* < \sim 100$ ms for the on-resonance pulse. In some cases, neither the EEP or EMP approach provide reliable performance (e.g., the m_y-component of the tanh pulse in Figure 6). In practice, if the EEP or EMP approaches are to be used, it is essential to select an appropriate time at which to calculate the initial amplitude and to consider potential errors that may result as a consequence of biased M_0 results produced for large B_1. The investigated on-resonance and chirp pulse are better suited for the EMP and EEP approaches, respectively.

To extend the range of conditions in which M_0 can be reliably estimated the MRDP approach proposes to update the forward modeling to directly include RDP, in which the magnitude of the relaxation terms in the Bloch equation is based on the estimated T_2^*. The MRDP scheme is shown to provide the most consistent RDP compensation over the largest range of B_1 and T_2^*, while also extending its functionality to other types of excitation pulses and all T_2^* scenarios. The improved RDP compensation provided by the MRDP scheme comes at the cost of increasing the complexity of the excitation modeling and requires several additional assumptions compared with the EEP and EMP approaches. Consider first the assumption of the T_2^* scenario. If only FID measurements are available, it is very difficult to determine reliably which regime is present. Although it is common to consider which T_2^* scenario is present when interpreting T_2^* (i.e., can T_2^* be used to gain insight into pore size and permeability or is it contaminated by T_{2IH}?), the standard forward model is not adjusted based on which regime is present. Neither the EEP or EMP approach modifies the excitation modeling based on T_2^* scenario, instead always solving the Bloch equation without relaxation terms present. However, Figure 3 clearly indicates that each regime can lead to different net transverse magnetizations (equivalent to affecting the signal amplitude and phase). An advantage of the MRDP approach is that it either allows insight into which T_2^* regime is present to be used to improve excitation modeling or provides the means to quantify uncertainty in the estimated profiles that originates from the fact that multiple excitation modeling approaches are consistent with the available data. We recommend that if no information about the T_2^* scenario is available, the data should be treated first as if the $T_2 \sim = T_2$ regime is present and then again as if the T_{2IH} dominated regime is present. By considering the two extreme cases, it may help provide insight into the uncertainty in the estimated water content and T_2^* profiles that stems from the way the excitation modeling is performed. Another potential advantage of being able to adjust the excitation modeling for different T_2^* regimes is that it may help provide insight into which T_2^* regime is present. For example, if modeling based on the $T_2 \sim = T_2^*$ regime can fit the data, whereas modeling based on the T_{2IH} dominated regime cannot, it may help provide valuable insight into the T_2-T_2^* relationship. An investigation into whether the MRDP approach can provide insight into which T_2^* regime is present will be the subject of future research.

The MRDP scheme also requires that T_1 be estimated, which is poorly constrained given that most surface NMR surveys only mea-

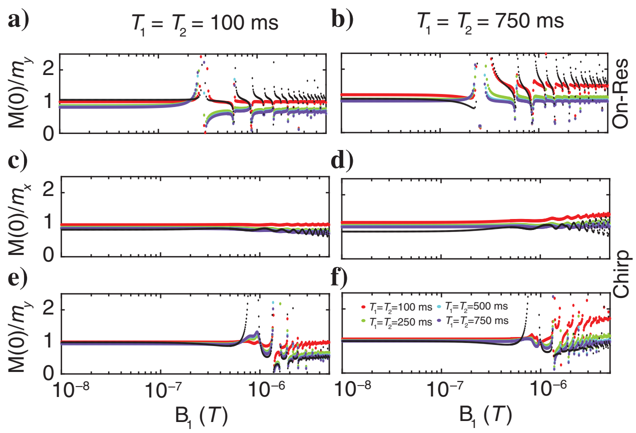

Figure 10. Sensitivity of the MRDP approach to the estimated value of T_1 and T_2 in the T_{2IH}-dominated regime. The top and bottom two rows correspond to the results for a 40 ms on-resonance pulse and a chirp pulse, respectively (same as in Figure 3). The left and right columns correspond to synthetic FIDs that were produced using $T_1 = T_2 = 100$ ms and $T_1 = T_2 = 750$ ms, respectively; $T_2^* = 40$ ms in all cases. The profile color corresponds to the estimated T_1 and T_2 (assumed $T_1 = T_2$) value used in the MRDP approach. The profile colors correspond to the T_1 value used in the MRDP approach. The T_1 values equal to 100 ms (red), 250 ms, 500 ms, and 750 ms (purple) were sampled. The black profile in the top row corresponds to the results that would be produced using the EMP approach, whereas the black profiles in the bottom two rows correspond to the results of the EEP approach.

sure FIDs and T_1 is generally unknown. For the $T_2 \sim T_2^*$ regime, the likely range of T_1 is roughly 1–3 times the magnitude of T_2^* (because we assume $T_2 = T_2^*$ in this limit). Values of T_1 larger than $3T_2^*$ are possible, but typical reservoir sediments commonly fall within the $1 - 3T_2$ range (Kleinberg and Farooqui, 1993). Poor T_1 estimates will degrade the reliability of the MRDP scheme. A conservative estimate of $T_1 = 2T_2^*$ was observed to provide a good balance, performing well in the $T_1 = T_2^*$ and $T_1 = 3T_2^*$ cases investigated in Figure 9. Similarly, in the $T_{2\mathrm{IH}}$-dominated regime, a moderate T_1 and T_2 estimate of 250 ms was also observed to balance performance for both cases considered in Figure 10. Despite the uncertainty about the true value of T_1, the MRDP scheme consistently provides improved performance compared to the EEP and EMP approaches even if T_1 is not estimated correctly. The MRDP scheme may also be performed multiple times for several estimates of T_1 to quantify the uncertainty that stems from an uncertain T_1 estimate. Alternatively, supplementary measurements, such as spin-echo, CPMG, or direct T_1 measurements, may be used to help constrain T_1 and improve the accuracy of the MRDP approach.

Several additional factors that may impact the reliability of the MRDP approach are the accuracy of the T_2^* and B_1 estimates, as well knowledge of the excitation pulse waveform. The T_2^* can be estimated directly from the observed decays, whereas an inversion is needed to estimate its value at each location in the subsurface. Errors in the estimated T_2^* value will reduce the accuracy of water content estimates produced by the MRDP approach. The T_2^* errors will also degrade the accuracy of the EEP and EMP approaches, in which the initial amplitude will be biased because of the extrapolation. Knowledge of B_1 at each location of the subsurface requires that the transmit loop geometry is known (ensured by careful deployment in the field) as well as an understanding of the subsurface conductivity structure. Inaccurate B_1 models will reduce the accuracy of the MRDP approach. However, a poor B_1 model will also affect surface NMR surveys using an EEP or EMP approach given that the entire surface NMR imaging procedure hinges on the accuracy of the B_1 model. The MRDP approach does not require T_2^* or B_1 characterization abilities beyond what is already available in every surface NMR measurement (but does depend on their reliability). The shape of the excitation waveform is well-known in practice, given that it is specified by the user and the actual current waveform in the transmit loop is measured. Therefore, the MRDP approach does not require characterization of the excitation pulse waveform beyond what is already available.

Returning to the EMP approach, this scheme was originally proposed in the context of an on-resonance pulse (Walbrecker et al., 2009). The breakdown of the EMP approach for the chirp pulse occurs because the perturbation of the magnetization is very different during a chirp pulse compared with an on-resonance pulse. This leads to different contributions of RDP to the final transverse magnetization. For example, at a small B_1 the magnetization spends much of the chirp pulse effectively oriented in the z-direction, where it is not exposed to T_2^* processes. Only toward the end of the pulse do the magnetizations at a small B_1 begin to develop large transverse components, thus limiting exposure to T_2^* processes and reducing RDP. In contrast, at a large B_1 the magnetization is rotated quickly into the transverse plane, where it spends much of the pulse locked in the x-direction increasing the exposure to T_2 processes potentially amplifying RDP. Comparing Figures 4 and 5 indicates that the EEP approach is better suited to the chirp pulse given that it more consistently produces an initial amplitude estimate consistent with the modeled transverse magnetization. However, the tanh pulse showed different behavior compared with the chirp pulse; the EMP approach performs better in some conditions for the tanh pulse. The differing behavior of the two investigated adiabatic pulses highlights that the performance of the EEP and EMP depends strongly on the excitation pulse waveform.

The performance of the EMP approach for the on-resonance case shown in Figure 5 displays results that differ slightly from those presented in Walbrecker et al. (2009). For example, Figure 5 demonstrates that the EMP approach breaks down at larger T_2^* and displays a strong dependence on B_1 and the T_2^* regime. Walbrecker et al. (2009) consider a scenario in which a $\pi/2$ on-resonance pulse was used (a single B_1 amplitude) for $T_2^* = T_2$ varying from 25 to 1000 ms, whereas T_1 was fixed at 1600 ms (i.e., the $T_2^* = T_2$ regime but with a long T_1). The source of the discrepancy between these two results is that region where the bias is most pronounced in the top row of Figure 5 is at B_1 greater than that considered in the Walbrecker et al. (2009) study. A second reason for the discrepancy is that the $T_2 \sim = T_2^*$ regime considered in this study used $T_2 = T_1$. In contrast, the T_1 value used by Walbrecker et al. (2009) ranges from 64 T_2 to 1.6 T_2.

Figures 4–10 all indicate that the large B_1 limit presents the most challenging situation to produce an accurate M_0 estimate; all three discussed approaches (EEP, EMP, MRDP) produce their largest biases at strong B_1. We hypothesize that the bias at large B_1 may contribute to difficulties describing the signal phase accurately for surface NMR inversions that handle complex data (Braun et al., 2005). For example, an on-resonance pulse produces the largest signal phases for the strongest pulse moments. This is due to the fact that the strongest pulse moments probe the greatest depths, at which the conductivity phase is largest. But large pulse moments also produce the strongest B_1, potentially exhibiting the greatest sensitivities to the biases observed in Figures 4–10. For the adiabatic pulse, the m_y-component appears to be the most challenging to estimate at a large B_1 (given its asymptotic behavior). A potential solution to limiting problems that may arise from the m_y-component for the adiabatic pulse is to reduce the amplitude of the rapidly oscillating portion of the m_y profile at a large B_1 (Figure 3g). Larger initial offsets between the transmit and Larmor frequency could help reduce the oscillation.

Note that the modeling for the $T_{2\mathrm{IH}}$-dominated regime in this work assumed that shape of the B_0 distribution is Lorentzian. If the signal loss due to $T_{2\mathrm{IH}}$ is to be considered an exponential decay, this requires that the B_0 distribution be Lorentzian (the Fourier transform of a decaying exponential in the time domain is a Lorentzian in the frequency domain). A Lorentzian B_0 distribution is common for reservoir sediments (Chen et al., 2005). If the B_0 distribution has an alternate shape (e.g., Gaussian), this would require that the observed decays be extrapolated in a different manner (Grunewald et al., 2012). The MRDP scheme could readily incorporate a different B_0 shape into the modeling. An advantage of the MRDP and EEP schemes compared with the EMP approach is that they reduce (or eliminate) the extrapolation time, which may help mitigate errors that arise from nonexponential decays (alternative B_0 distribution shapes).

The presented examples deal with mono-exponential fits to the observed FIDs. This approach is commonly used by inversion schemes that assign each depth layer a single T_2^* value. Alternative inversion schemes can also be used to produce a relaxation time distribution within each depth layer. To model the expected RDP in this case, an approach similar to the modeling for the Larmor frequency distribution (the inhomogeneous magnetic field case) can be used. Equation 5 would instead have a double sum, one that sums over the different Larmor frequencies and another that sums over the different relaxation times. The coefficients in the relaxation time sum would be determined by the relative abundance of each relaxation time (i.e., the amplitude of the relaxation time distribution at that value). Although the proposed scheme is presented for free induction decay measurements, in principle, it should be possible to extend its functionality to multipulse experiments as well.

Integration of the MRDP scheme into the surface NMR workflow will likely require a protocol similar to surface NMR T_1 inversions (Müller-Petke et al., 2013), where the current estimate of T_1 distribution is used to form an updated kernel and improve the results iteratively. In this case, the current T_2^* estimates would be used to improve the ability of the forward model to more robustly reproduce the initial amplitudes estimates given the correct water. Integration of the proposed MRDP approach into the surface NMR workflow will be the subject of future research.

CONCLUSION

RDP effects have a complex dependence on B_1, T_2^*, the T_2^* scenario, and the excitation pulse waveform. Both investigated excitation pulse types (on-resonance and adiabatic pulses) are shown to result in different net excitations depending on which T_2^* regime is present (i.e., homogeneous [$T_2 \sim = T_2^*$] versus inhomogeneous B_0 [T_{2IH} dominated]), with the differences being greatest at small T_2^* and large B_1. Standard approaches to compensate for RDP (EEP and EMP), which involve excitation modeling that solves the Bloch equation without relaxation terms present, do not adjust excitation modeling based on the observed T_2^* or the estimated T_2^* scenario. Instead, RDP is compensated by adjusting the time at which the initial amplitude is calculated. The EEP and EMP approaches are shown to break down in the fast T_2^* and large B_1 limits, and they require excitation-pulse-specific time zeros. For example, the EMP approach worked well for the on-resonance pulse but not for the chirp pulse, whereas the EEP approach worked well for the chirp pulse but not the on-resonance pulse. Note that the EEP approach is not better than the EMP approach for adiabatic pulses in general (as demonstrated by the hyperbolic tangent pulse). In summary, if excitation modeling ignores the relaxation terms in the Bloch equation, one must ensure that the time at which the initial amplitude is calculated is appropriate for the specific excitation pulse to be used.

To provide a more flexible protocol capable of expanding the range of T_2^* and B_1 where reliable water contents can be produced, while also extending functionality to arbitrary excitation pulses and all T_2^* regimes, an approach involving excitation modeling that includes relaxation terms is presented (the MRDP approach). The proposed scheme uses estimates of the observed T_2^* values to directly include RDP effects in the modeling, allowing the flexibility to appropriately weight RDP depending on specific T_2^*, B_1, T_2^* scenario, and excitation pulse waveform. However, the MRDP approach requires T_1 and the T_2^* scenario to be estimated. Despite the requirement of additional assumptions in the excitation modeling (which are poorly constrained), the MRDP approach is observed to extend the range of T_2^* and B_1, where a reliable M_0 estimate can be produced, even for a poor T_1 estimate. The MRDP approach also offers the ability to adjust the excitation modeling based on the T_2^* scenario. This may help quantify uncertainty in the estimated water content and T_2^* profiles that stems from ambiguity about how the excitation modeling should be performed (given that the T_2^* scenario is unknown). Given only FID measurements, data should be treated as if both T_2^* regimes may be present. The proposed MRDP approach has great potential to allow the surface NMR forward model to better account for RDP; its integration into the surface NMR inversion framework will be the subject of future work.

ACKNOWLEDGMENTS

D. Grombacher was supported by funding from a Danish Council for Independent Research Postdoctoral Grant (DFF-5051-00002). A. Behroozmand was supported by funding from the Danish Council for Independent Research.

REFERENCES

Behroozmand, A. A., E. Auken, G. Fiandaca, and A. V. Christiansen, 2012, Improvement in MRS parameter estimation by joint and laterally constrained inversion of MRS and TEM data: Geophysics, **77**, no. 4, WB191–WB200, doi: 10.1190/geo2011-0404.1.
Bloch, F., 1946, Nuclear induction: Physical Review, **70**, 460, doi: 10.1103/PhysRev.70.460.
Braun, M., M. Hertrich, and U. Yaramanci, 2005, Study on complex inversion of magnetic resonance sounding signals: Near Surface Geophysics, **3**, 155–163, doi: 10.3997/1873-0604.2005011.
Brownstein, K. R., and C. E. Tarr, 1979, Importance of classical diffusion in NMR studies of water in biological cells: Physical Review A, **19**, 2446–2453, doi: 10.1103/PhysRevA.19.2446.
Chen, Q., A. E. Marble, B. G. Colpitts, and B. J. Balcom, 2005, The internal magnetic field distribution, and single exponential magnetic resonance free induction decay, in rocks: Journal of Magnetic Resonance, **175**, 300–308, doi: 10.1016/j.jmr.2005.05.001.
Costabel, S., and U. Yaramanci, 2011a, Relative hydraulic conductivity and effective saturation from Earth's field nuclear magnetic resonance — A method for assessing the vadose zone: Near Surface Geophysics, **9**, 155–167, doi: 10.3997/1873-0604.2010055.
Costabel, S., and U. Yaramanci, 2011b, Relative hydraulic conductivity in the vadose zone from magnetic resonance sounding — Brooks-Corey parameterization of the capillary fringe: Geophysics, **76**, no. 3, G61–G71, doi: 10.1190/1.3552688.
Gershenzon, N. I., K. Kobzar, B. Luy, S. J. Glaser, and T. E. Skinner, 2007, Optimal control design of excitation pulses that accommodate relaxation: Journal of Magnetic Resonance, **188**, 330–336, doi: 10.1016/j.jmr.2007.08.007.
Grombacher, D., and R. Knight, 2015, The impact of off-resonance effects on water content estimates in surface nuclear magnetic resonance: Geophysics, **80**, no. 6, E329–E342, doi: 10.1190/geo2014-0402.1.
Grombacher, D., M. Müller-Petke, and R. Knight, 2016, Frequency-cycling for compensation of undesired off-resonance effects in surface NMR: Geophysics, **81**, no. 4, WB33–WB48, doi: 10.1190/geo2015-0181.1.
Grombacher, D., J. O. Walbrecker, and R. Knight, 2014, Imparting a phase during excitation for improved resolution in surface nuclear magnetic resonance: Geophysics, **79**, no. 6, E329–E339, doi: 10.1190/geo2013-0452.1.
Grunewald, E., D. Grombacher, and D. O. Walsh, 2016, Adiabatic pulses enhance surface nuclear magnetic resonance measurements and survey speed for groundwater investigations: Geophysics, **81**, no. 4, WB85–WB96, doi: 10.1190/geo2015-0527.1.
Grunewald, E., and R. Knight, 2011, The effect of pore size and magnetic susceptibility on the surface NMR relaxation parameter T_2^*: Near Surface Geophysics, **9**, 169–178, doi: 10.3997/1873-0604.2010062.
Grunewald, E., and R. Knight, 2012, Nonexponential decay of the surface-NMR signal and implications for water content estimation: Geophysics, **77**, no. 1, EN1–EN9, doi: 10.1190/geo2011-0160.1.
Grunewald, E., R. Knight, and D. Walsh, 2014, Advancement and validation of surface nuclear magnetic resonance spin-echo measurements of T_2: Geophysics, **79**, no. 2, EN15–EN23, doi: 10.1190/geo2013-0105.1.
Grunewald, E., and D. O. Walsh, 2013, Multiecho scheme advances surface NMR for aquifer characterization: Geophysical Review Letters, **40**, 6346–6350, doi: 10.1002/2013GL057607.
Hajduk, P. J., D. A. Horita, and L. E. Lerner, 1993, Theoretical analysis of relaxation during shaped pulses. 1. The effects of short T_1 and T_2: Journal of Magnetic Resonance, **103**, 40–52, doi: 10.1006/jmra.1993.1129.

Kenyon, W. E., P. Day, C. Straley, and J. F. Willemsen, 1988, A three-part study of NMR longitudinal relaxation properties of water saturated sandstones: SPE Formation Evaluation, **3**, 622–636, doi: 10.2118/15643-PA.

Kleinberg, R. L., and S. A. Farooqui, 1993, T_1/T_2 ratio and frequency dependence of NMR relaxation in porous sedimentary rocks: Journal of Colloid and Interface Science, **158**, 195–198, doi: 10.1006/jcis.1993.1247.

Legchenko, A., 2005, Improved modelling of the magnetic resonance signal in the presence of shallow aquifers: Near Surface Geophysics, **3**, 121–130, doi: 10.3997/1873-0604.2005008.

Legchenko, A., J. M. Baltassat, A. Bobachev, C. Martin, H. Robain, and J. M. Vouillamoz, 2004, Magnetic resonance sounding applied to aquifer characterization: Ground Water, **42**, 363–373, doi: 10.1111/j.1745-6584.2004.tb02684.x.

Legchenko, A., and P. Valla, 2002, A review of the basic principles for proton magnetic resonance sounding measurements: Journal of Applied Geophysics, **50**, 3–19, doi: 10.1016/S0926-9851(02)00127-1.

Legchenko, A., J. M. Vouillamoz, and J. Roy, 2010, Applications of the magnetic resonance sounding method to the investigation of aquifers in the presence of magnetic materials: Geophysics, **75**, no. 6, L91–L100, doi: 10.1190/1.3494596.

Li, T., L.-B. Feng, Q.-M. Duan, J. Lin, X.-F. Yi, C.-D. Jiang, and S.-Y. Li, 2015, Research and realization of short dead-time surface nuclear magnetic resonance for groundwater exploration: IEEE Transactions on Instrumentation and Measurement, **64**, 278–287, doi: 10.1109/TIM.2014.2338693.

Mohnke, O., and U. Yaramanci, 2008, Pore size distributions and hydraulic conductivities of rocks derived from magnetic resonance sounding relaxation data using multi-exponential decay time inversion: Journal of Applied Geophysics, **66**, 73–81, doi: 10.1016/j.jappgeo.2008.05.002.

Müller-Petke, M., J. O. Walbrecker, and R. Knight, 2013, The inversion of surface-NMR T_1 data for improved aquifer characterization: Geophysics, **78**, no. 6, EN83–EN94, doi: 10.1190/geo2013-0035.1.

Norris, D. G., H. Ludemann, and D. Leibfritz, 1991, An analysis of the effects of short T_2 values on the hyperbolic secant pulse: Journal of Magnetic Resonance, **92**, 94–101.

Nuzillard, J.-M., and R. Freeman, 1993, Band-selective pulses designed to accommodate relaxation: Journal of Magnetic Resonance, **107**, 113–118, doi: 10.1006/jmra.1994.1056.

Raddi, A., and U. Klose, 2000, Relaxation effects on transverse magnetization using RF pulses long compared to T_2: Journal of Magnetic Resonance, **144**, 108–114.

Roy, J., A. Rouleau, M. Chouteau, and M. Bureau, 2008, Widespread occurrence of aquifers currently undetectable with the MRS technique in the Grenville geological province: Journal of Applied Geophysics, **66**, 82–93, doi: 10.1016/j.jappgeo.2008.04.006.

Schirov, M., A. Legchenko, and G. Creer, 1991, A new direct non-invasive groundwater detection technology for Australia: Exploration Geophysics, **22**, 333–338, doi: 10.1071/EG991333.

Sen, P. N., C. Straley, W. E. Kenyon, and M. S. Whittingham, 1990, Surface to volume ratio, charge density, nuclear magnetic relaxation and permeability in clay bearing sandstones: Geophysics, **55**, 61–69, doi: 10.1190/1.1442772.

Shen, J., and L. E. Lerner, 1994, Selective radiofrequency pulses minimizing relaxation: Journal of Magnetic Resonance, **112**, 265–269, doi: 10.1006/jmra.1995.1044.

Shushakov, O. A., 1996a, Groundwater NMR in conductive water: Geophyiscs, **61**, 998–1006, doi: 10.1190/1.1444048.

Shushakov, O. A., 1996b, Surface NMR measurement of proton relaxation times in medium to coarse-grained sand aquifer: Magnetic Resonance Imaging, **14**, 959–960, doi: 10.1016/S0730-725X(96)00194-4.

Tannus, A., and M. Garwood, 1997, Adiabatic pulses: NMR in Biomedicine, **10**, 423–434, doi: 10.1002/(ISSN)1099-1492.

Trushkin, D. V., O. A. Shushakov, and A. V. Legchenko, 1995, Surface NMR applied to an electroconductive medium: Geophysical Prospecting, **43**, 623–633, doi: 10.1111/j.1365-2478.1995.tb00271.x.

Walbrecker, J. O., M. Hertrich, and A. G. Green, 2009, Accounting for relaxation during pulse effects in surface NMR data: Geophysics, **74**, no. 6, G27–G34, doi: 10.1190/1.3238366.

Walbrecker, J. O., M. Hertrich, and A. G. Green, 2011a, Off-resonance effects in surface nuclear magnetic resonance: Geophysics, **76**, no. 2, G1–G12, doi: 10.1190/1.3535414.

Walbrecker, J. O., M. Hertrich, J. A. Lehmann-Horn, and A.G. Green, 2011b, Estimating the longitudinal relaxation time T_1 in surface NMR: Geophysics, **76**, no. 2, F111–F122, doi: 10.1190/1.3549642.

Walsh, D. O., E. Grunewald, P. Turner, A. Hinnell, and P. Ferre, 2011, Practical limitations and applications of short dead time surface NMR: Near Surface Geophysics, **9**, 103–111, doi: 10.3997/1873-0604.2010073.

Weichman, P. B., E. M. Lavely, and M. H. Ritzwoller, 2000, Theory of surface nuclear magnetic resonance with applications to geophysical imaging problems: Physical Review E, **62**, 1290–1312, doi: 10.1103/PhysRevE.62.1290.